Asymptotic modelling and direct numerical simulations of multilayer pressure-driven flows

A. Kalogirou[a,b], R. Cimpeanu[c,d,e], M. G. Blyth[a]

[a]*School of Mathematics, University of East Anglia, Norwich Research Park, Norwich NR4 7TJ, United Kingdom*
[b]*School of Mathematical Sciences, University of Nottingham, University Park, Nottingham NG7 2RD, United Kingdom*
[c]*Mathematical Institute, University of Oxford, Oxford OX2 6GG, United Kingdom*
[d]*Department of Mathematics, Imperial College London, South Kensington Campus, London SW7 2AZ, United Kingdom*
[e]*Mathematics Institute, University of Warwick, Coventry CV4 7AL, United Kingdom*

Abstract

The nonlinear dynamics of two immiscible superposed viscous fluid layers in a channel is examined using asymptotic modelling and direct numerical simulations (DNS). The flow is driven by an imposed axial pressure gradient. Working on the assumption that one of the layers is thin, a weakly-nonlinear evolution equation for the interfacial shape is derived that couples the dynamics in the two layers via a nonlocal integral term whose kernel is determined by solving the linearised Navier-Stokes equations in the thicker fluid. The model equation incorporates salient physical effects including inertia, gravity, and surface tension, and allows for comparison with DNS at finite Reynolds numbers. Direct comparison of travelling-wave solutions obtained from the model equation and from DNS show good agreement for both stably and unstably stratified flows. Both the model and the DNS indicate regions in parameter space where unimodal, bimodal and trimodal waves co-exist. Nevertheless, the asymptotic model cannot capture the dynamics for a sufficiently strong unstable density stratification when interfacial break-up and eventual dripping occurs. In this case, complicated interfacial dynamics arise from the dominance of the gravitational force over the shear force due to the underlying flow, and this is investigated in detail using DNS.

Keywords: interfacial instability, multilayer flow, Poiseuille flow, thin films, direct numerical simulation

1. Introduction

Pressure-driven flows are of central importance in numerous contexts, ranging from industrial applications such as polymer extrusion [1], oil transport and microfluidics, to applications in biology, e.g. fluid feeding in insects [2], haemodynamics, pulmonary flow and lung transport [3]. Understanding pressure-driven flow is also helpful for studying the flow in flexible tubes, or tubes with variable radius such as an obstructed artery. In certain scenarios the flow may involve multiple fluid layers making it susceptible to interfacial instabilities: the Rayleigh-Taylor instability that occurs when a heavier fluid lies above a lighter fluid [4], instability due to viscosity stratification that occurs when the most viscous fluid layer is also the thinnest (the so-called thin-layer effect) [5], and shear-driven instability which can drive the transition to turbulence [6].

Interfacial instability in a flow of superposed fluids was first observed experimentally by Charles and Lilleleht [6], and later by Kao and Park [7], in their experiments on two-layer Poiseuille flow in a channel – the authors were interested in investigating laminar-turbulent transitions by looking at the structure of the interface, but it was unclear which mechanism was responsible for the manifestation of the observed interfacial instability. A linear stability analysis of this flow was first carried out by Yih [8], who confined his attention to long-wave disturbances and identified an interfacial instability due to viscosity stratification. A more general linear analysis for disturbances of arbitrary wavelength was performed numerically by Yiantsios and Higgins [9], who noted that the unstable interfacial waves seen in the experiments [6, 7] are due to a shear mode of the Tollmien-Schlichting type rather than to a long-wave Yih mode. Yiantsios and Higgins [10] later extended Yih's work to include the effect of density and layer thickness ratio. In related work, Blennerhassett [11] performed a linear stability analysis for Couette-Poiseuille flow, and Hooper [12] discussed the similarities between the stability properties of two-layer Poiseuille flow and Couette-Poiseuille flow. The stability of three-layer Poiseuille flow to disturbances of arbitrary wavelength was investigated numerically by Renardy [13], who also commented on the similarities with Hagen-Poiseuille flow in a pipe. For multilayer Poiseuille flow with more than two fluid layers, Anturkar et al. [14] reported the conditions for linear instability via an analytical treatment for long- or short-wavelength perturbations, as well as numerical computations for disturbances of arbitrary wavelength.

A number of asymptotic models have been developed to study the nonlinear evolution of multilayer flows. Tilley et al. [15, 16] investigated the linear stability of a laminar two-fluid Poiseuille flow in an inclined channel and derived a long-wave nonlinear equation for the evolution of the interface (which reduces to the well-known Kuramoto-Sivashinsky equation in the weakly-nonlinear limit). The evolution of finite-amplitude disturbances was studied by Power et al. [17] using a boundary-layer approximation that allowed for both viscosity and density stratification. They found that both stable and unstable flow configurations are possible in the presence of weak or moderate inertia, respectively. Kliakhandler and Sivashinsky [18] derived a weakly nonlinear model for multilayer pressure-driven flow and reported the possibility of obtaining different flow behaviour depending on the initial condition, for example the emergence of soliton-like structures and quasi-periodic waves. Sangalli et al. [19] examined the onset, growth and saturation of short waves at the interface of a co-current stratified gas-liquid flow both experimentally and using weakly-nonlinear theory. Recently, Alba et al. [20] used a weighted residual approach to investigate a two-layer thin-film flow in a channel assuming equal-density fluids and ignoring the effect of surface tension. They found that interfacial waves either decay or grow downstream depending on the type of perturbation that is imposed on the base flow. To our knowledge, no previous studies have considered the case of a small layer thickness ratio, namely a thin film beside a much thicker fluid layer. This problem is of great relevance in industry as a thin film can be controlled into a desired state depending on the application [21] – for example, in coating flows it is beneficial to have a flat interface, while in mass transport applications interfacial waves may be advantageous.

While there exist a limited number of studies that use direct numerical simulations (DNS) to investigate instabilities in multilayer channel flows, in the vast majority of cases there are significant restrictions on the fluid properties and on the flow structures that can develop. Cao et al. [22] and Zhang et al. [23] used front-tracking methods to examine two-layer flow in a channel. Cao et al. [22] assumed equal densities but allowed for different viscosities. The dynamics were limited to the case of small to moderate Reynolds number and the computations were compared with theory for the early stages of evolution of an unstable flow. Zhang et al. [23] allowed for different density fluids in a stably stratified configuration, and also for an angle of inclination between the channel and the horizontal. Gada and Sharma [24] carried out computations for a similar fluid system using the level-set

method and concentrated on the transition from steady to unsteady flow configurations, taking into account variations in interfacial height and other physical properties (velocity, surface tension, gravity). Valluri et al. [25] used a diffuse-interface method to distinguish between absolute and convective instability regimes in laminar two-layer channel flows. Using this method they were able to describe the emergence of liquid fingers due to viscosity stratification (for same-density fluids). While the aforementioned studies have shed light on different aspects of the rich flow behaviour to be expected in these systems, to the best of our knowledge none have examined the regime in which gravity-driven instabilities compete directly with the streamwise flow leading to the possibility of interfacial break-up.

In the present work, we examine the nonlinear dynamics of two-layer pressure-driven flows in the case when one of the fluid layers is much thinner than the other. The thin-film approximation considered here is relevant to numerous industrial applications such as oil transport and mass-transfer operations. We restrict attention to two-dimensional disturbances which is fully justified at least for stably stratified systems due to the existence of a Squire's theorem [10, 26, 27] – but note that we will also consider unstably stratified configurations in which case three-dimensional disturbances would be appropriate. We perform a weakly nonlinear analysis to extend the work presented in Kalogirou et al. [28] for Couette flow to the present case of Poiseuille flow, also allowing for a density contrast. The result is an evolution equation that describes the dynamics of the thin film and which depends on three key parameters that capture the relative effects of gravity, viscosity stratification and inertia. Inertia comes into play via a nonlocal term that couples the dynamics between the layers through the solution of an Orr-Sommerfeld problem which depends on the Reynolds number in the thicker fluid. The model equation can be used as a valuable tool to quickly explore the nonlinear dynamics and to tease out the important physical mechanisms. DNS can also be used to map out the dynamics, but these are highly challenging computationally, given the disparity in thickness between the two fluid layers and the natural streamwise lengthscale on which disturbances evolve. Nonetheless we carry out a selection of direct numerical simulations in order to establish the range of validity of the weakly-nonlinear model equation. Using the model equation, we provide conditions for linear stability of the flow that agree with previous results [10]. Furthermore, we compute saturated travelling-wave solutions numerically and demonstrate the co-existence of multiple solutions, a phenomenon which has been reported before in re-

lated experimental [29] and theoretical studies [28]. Finally, we present DNS results for increased density contrasts, providing evidence of more intricate time-periodic structures and leading to eventual film rupture for extreme density differences.

The structure of the paper is as follows. Section 2 presents the governing equations and the derivation of the weakly nonlinear evolution equation for the interface. Section 3 provides computational details of the simulations for both the model and the DNS. In Section 4, the linear stability properties of the problem are described and numerical results of the model equation are presented together with comparisons against direct numerical simulations. A summary of the main results can be found in Section 5.

2. Weakly nonlinear evolution equation

Consider two superposed viscous fluids of different densities ρ_1, ρ_2 and viscosities μ_1, μ_2 occupying a horizontal channel with fixed height d. The geometry of the problem is described in Cartesian coordinates (x, y) as shown in Figure 1, with subscript notation 1 and 2 henceforth referring to the lower and upper fluid, respectively. The fluids are immiscible and are separated by an interface at $y = h(x, t)$, and they are also subject to the action of gravity $\boldsymbol{g} = (0, -g)$. The pressure in each fluid region is denoted by $p_i(x, y, t)$, $i = 1, 2$, and the flow velocity by $\boldsymbol{u}_i(x, y, t)$, with horizontal and vertical velocity components $u_i(x, y, t)$, $v_i(x, y, t)$, respectively. A flow is generated in the channel by applying a constant pressure gradient $G^* = -p_{ix}$, such that the pressure drop in a horizontal domain of length L is $\Delta p_i \equiv p_i(x = 0) - p_i(x = L) > 0$ in each fluid $i = 1, 2$.

The problem is expressed in non-dimensional form by rescaling lengths with the channel height d, velocities with the maximum fluid velocity U of the unidirectional base flow (to be defined below), pressures with $\rho_1 U^2$, and time with d/U. Furthermore, the following non-dimensional parameters are introduced: the density and viscosity ratios,

$$r = \frac{\rho_2}{\rho_1}, \quad m = \frac{\mu_2}{\mu_1}, \tag{1}$$

(we also define $r_i = \rho_i/\rho_1$ and $m_i = \mu_i/\mu_1$, $i = 1, 2$, such that $r_1 = 1$, $r_2 = r$ and $m_1 = 1$ and $m_2 = m$), the *Reynolds number* in each fluid,

$$Re \equiv Re_1 = \frac{\rho_1 U d}{\mu_1}, \quad Re_2 = \frac{\rho_2 U d}{\mu_2} = \frac{r}{m} Re, \tag{2}$$

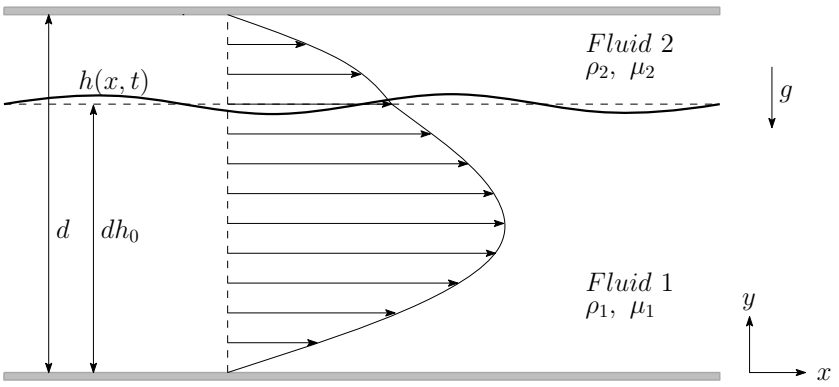

Figure 1: Geometry of the problem in Cartesian coordinates (x, y): two superposed fluid layers fill a long channel of height d, separated by an interface at $y = h(x, t)$ and driven by an imposed horizontal pressure gradient G^*. Gravity g also acts in the negative y-direction.

the *Froude number*, *capillary number*, and *Bond number*,

$$Fr = \frac{U}{\sqrt{gd}}, \quad Ca = \frac{\mu_2 U}{\gamma}, \quad Bo = \frac{(1-r)d^2\rho_1 g}{\gamma}, \tag{3}$$

where γ is the interfacial tension.

In the steady state, the interface between the fluids is planar at $y = h_0$. The base two-fluid Poiseuille flow is described by

$$\bar{u}_1(y) = -Ay^2 + By, \qquad \bar{u}_2(y) = -\frac{A}{m}y^2 + \frac{B}{m}y + C, \tag{4a}$$

$$\bar{v}_1 = \bar{v}_2 = 0, \tag{4b}$$

$$\bar{p}_i(x, y) = -\frac{r_i}{Fr^2}(y - h_0) - Gx, \qquad i = 1, 2, \tag{4c}$$

where overbars denote the base state and the coefficients A, B, C are given by

$$A = \frac{1}{2}ReG, \quad B = A\left(\frac{1 + h_0^2(m-1)}{1 + h_0(m-1)}\right), \tag{4d}$$

$$C = A\left(\frac{m-1}{m}\right)\left(\frac{h_0(1-h_0)}{1 + h_0(m-1)}\right), \tag{4e}$$

with $G = G^*d/\rho_1 U^2 > 0$ the dimensionless pressure gradient. In the thin-film limit considered in this work, the maximum velocity of the base flow is

achieved in the thicker fluid layer and is given below in dimensional form (as used in the non-dimensionalisation)

$$U = U_{max} = \frac{G^* d^2}{8\mu_1} \left(\frac{1 + h_0^2(m-1)}{1 + h_0(m-1)} \right)^2 . \tag{5}$$

The flow in each fluid region $i = 1, 2$ satisfies the non-dimensional Navier-Stokes equations and the continuity equation, as well as no-slip and no-penetration conditions at the two walls,

$$\boldsymbol{u}_{it} + (\boldsymbol{u}_i \cdot \nabla)\boldsymbol{u}_i = -\frac{1}{r_i}\nabla p_i + \frac{m_i}{r_i Re}\nabla^2 \boldsymbol{u}_i - \boldsymbol{F}, \qquad \nabla \cdot \boldsymbol{u}_i = 0, \tag{6a}$$

$$\boldsymbol{u}_1 = (0,0) \quad \text{at} \quad y = 0, \qquad \boldsymbol{u}_2 = (0,0) \quad \text{at} \quad y = 1, \tag{6b}$$

with $\boldsymbol{F} = (0, 1/Fr^2)$. Appropriate coupling conditions are required at the interface, namely continuity of fluid velocities

$$\boldsymbol{u}_1 = \boldsymbol{u}_2 \quad \text{at} \quad y = h(x,t), \tag{7}$$

a jump condition on the stress, decomposed into its tangential and normal components, given by

$$\Big[4m_i h_x u_{ix} + m_i \left(h_x^2 - 1 \right) \left(u_{iy} + v_{ix} \right) \Big]_2^1 = 0, \tag{8a}$$

$$\Big[-p_i \left(1 + h_x^2 \right) + \frac{2m_i}{Re} \Big(h_x^2 u_{ix} + v_{iy} - h_x \left(u_{iy} + v_{ix} \right) \Big) \Big]_2^1 = -\frac{m}{Ca\,Re} \frac{h_{xx}}{\sqrt{1 + h_x^2}}, \tag{8b}$$

at $y = h(x,t)$, and the kinematic boundary condition

$$v_1 = h_t + u_1 h_x \quad \text{at} \quad y = h(x,t). \tag{9}$$

The main aim in this study is to investigate the evolution of the flow when one of the fluids is thin, and we take this to be the upper fluid. In many applications it is required to generate interfacial waves in order to enhance mass transport; this is typically achieved by introducing arbitrary disturbances to the interface and finding specific parametric sets that support instability of these disturbances. Here we are interested in the early stages of the instability when the disturbances are small and we will accordingly

derive a weakly nonlinear equation for the evolution of the film thickness perturbation. Following the work of Bassom et al. [30], Kalogirou et al. [28] and Kalogirou [31], we proceed by introducing a perturbation to the interface defined by

$$h(x,t) = h_0 - \epsilon^2 \tilde{h}(x,t), \quad \text{with} \quad h_0 = 1-\epsilon,\ \tilde{h} = \mathcal{O}(1) \quad \text{and} \quad \epsilon \ll 1. \tag{10}$$

For convenience, the new variable $\xi = (1-y)/\epsilon$ is introduced in the thin upper fluid. The flow is perturbed away from the base state (4) by writing

$$u_1 = \bar{u}_1(y) + \epsilon^2\, \tilde{u}_1(x,y,t) + \cdots, \qquad v_1 = \epsilon^2\, \tilde{v}_1(x,y,t) + \cdots, \tag{11a}$$

$$p_1 = \bar{p}_1(x,y) + \epsilon^2\, \tilde{p}_1(x,y,t) + \cdots, \tag{11b}$$

in the thick fluid 1, while in the thin fluid 2 we expand as

$$u_2 = \bar{u}_2(\xi) + \epsilon^3\, \tilde{u}_2(x,\xi,t) + \cdots, \qquad v_2 = \epsilon^4\, \tilde{v}_2(x,\xi,t) + \cdots, \tag{11c}$$

$$p_2 = \bar{p}_2(x,\xi) + \epsilon\, \tilde{p}_2(x,\xi,t) + \cdots, \tag{11d}$$

with all perturbation variables $\tilde{u}_i$, $\tilde{v}_i$, $\tilde{p}_i$, $i = 1, 2$, of $\mathcal{O}(1)$. The above expansions arise by conducting a careful scaling analysis (see Papageorgiou et al. [32], Kalogirou [33]) that reveals the appropriate scales necessary to retain nonlinearity and other physical effects of interest such as inertia and interfacial tension in the evolution equation. We also note that, unless otherwise stated, all non-dimensional variables including the density ratio, viscosity ratio and Reynolds number are assumed to be of $\mathcal{O}(1)$.

In what follows, the main steps of the asymptotic model derivation are outlined, but we refer the reader to Bassom et al. [30], Kalogirou et al. [28] and Kalogirou [31] for more details. The film thickness evolution equation is obtained from the leading-order kinematic condition (9), cast below in (13) into a frame of reference moving with the undisturbed interfacial velocity and a slow time, according to the rescalings

$$\tilde{x} = x - \bar{u}_2(1-\epsilon)\, t, \qquad \tilde{t} = \epsilon^2 t, \tag{12}$$

and given by

$$\tilde{h}_{\tilde{t}} + \frac{4}{m}\tilde{h}\tilde{h}_{\tilde{x}} = -\tilde{v}_2\big|_{\xi=1}. \tag{13}$$

The term on the right hand side of (13) can be found by solving the momentum equations in the film, which are hitherto simplified to the lubrication equations due to the flow expansions introduced earlier.

The leading-order normal stress balance at the interface (8b) is used to obtain the pressure in the thin fluid, and the capillary number is rescaled as $Ca = \epsilon\tilde{Ca}$, with $\tilde{Ca} = \mathcal{O}(1)$, in order to retain strong surface tension effects. The pressure is used in the solution of the momentum equation for the horizontal velocity $\tilde{u}_2$ in the thin film, which also utilises the leading-order tangential stress balance (8a)as a boundary condition. Employing the continuity equation then yields an expression for the vertical velocity in the film, evaluated at the interface as it is required in (13),

$$\tilde{v}_2\big|_{\xi=1} = \frac{1}{3\tilde{Ca}}(\tilde{h}_{\tilde{x}\tilde{x}\tilde{x}\tilde{x}} - Bo\,\tilde{h}_{\tilde{x}\tilde{x}}) - \frac{1}{2m}\mathcal{U}\big|_{y=1}. \tag{14}$$

The term $\mathcal{U}(\tilde{x}, y) = \tilde{u}_{1\tilde{x}y} + \tilde{v}_{1\tilde{x}\tilde{x}}$ originates from the tangential stress balance; it provides coupling between the fluid velocities in each layer and is the source of nonlocality in the final evolution equation. It is found by solving the problem in the lower layer, as described below.

Applying the relevant flow perturbations in the thick fluid layer, as well as the slow-time scale and moving frame of reference (12) (see also Kalogirou [31]) results in the steady linearised Navier-Stokes equations. These are written in Fourier space and pressure is eliminated, to give an Orr-Sommerfeld-type equation for the vertical velocity in the lower fluid, $\hat{v}_1$ (where a hat stands for Fourier transform). The following boundary value problem is hence obtained

$$\left(\mathcal{V}^{(iv)} - 2k^2\mathcal{V}'' + k^4\mathcal{V}\right) - ikRe\left(\bar{u}_1\left(\mathcal{V}'' - k^2\mathcal{V}\right) - \frac{d^2\bar{u}_1}{dy^2}\mathcal{V}\right) = 0, \tag{15a}$$

$$\mathcal{V}(0) = \mathcal{V}'(0) = 0, \qquad \mathcal{V}(1) = 0,\ \mathcal{V}'(1) = 1, \tag{15b}$$

for the rescaled velocity $\mathcal{V}(y)$, defined by

$$\hat{v}_1(y) = -4ik\left(\frac{1}{m} - 1\right)\hat{h}\mathcal{V}(y), \tag{16}$$

with the four boundary conditions (15b) arising from the requirement of the no-slip and no-penetration conditions at the lower wall, and the requirement for velocity continuity at the interface. The nonlocal term $\mathcal{U}(\tilde{x}, y) = \tilde{u}_{1\tilde{x}y} + \tilde{v}_{1\tilde{x}\tilde{x}}$ in (14) can be then evaluated, first in Fourier space through

$$\hat{\mathcal{U}}\big|_{y=1} = -\frac{d^2\hat{v}_1}{dy^2}\Big|_{y=1} - k^2\hat{v}_1(1) = 4ik\left(\frac{1}{m} - 1\right)\hat{h}\mathcal{V}''(1), \tag{17}$$

and afterwards in real space by applying inverse Fourier transform.

Finally, equation (13) is canonically rescaled by applying the transformations

$$\tilde{h} = \frac{m}{12\tilde{Ca}}\eta, \quad \tilde{t} = 3\tilde{Ca}\,\tau, \quad \tilde{x} = \chi, \tag{18}$$

and the following evolution equation for the film thickness perturbation is obtained

$$\eta_\tau + \eta\eta_\chi - Bo\,\eta_{\chi\chi} + \eta_{\chi\chi\chi\chi} + i\mu\left(\frac{1}{2\pi}\int_{-\infty}^{+\infty}\mathcal{N}(k;Re)\,\hat{\eta}(k)\,\mathrm{e}^{ik\chi}\,dk\right) = 0, \tag{19}$$

where the kernel $\mathcal{N}(k;Re)$ is given by

$$\mathcal{N}(k;Re) = k\mathcal{V}''(1), \tag{20}$$

and depends implicitly on the Reynolds number in the lower fluid through the solution of $\mathcal{V}$ from (15). The model evolution equation (19) is a nonlocal Kuramoto-Sivashinsky-type equation and involves three key parameters: the Reynolds number, Re, represents the effects of inertia and viscous effects in the thick fluid layer; the Bond number, Bo (defined in (3)), represents the effect of density stratification; and the viscosity-stratification parameter, μ, defined by

$$\mu = 6\,\tilde{Ca}\left(\frac{m-1}{m^2}\right). \tag{21}$$

The Bond number is responsible for instabilities in cases when the upper fluid is the heavier (corresponding to $Bo < 0$), while parameter μ causes destabilisation when the thin fluid is the more viscous (i.e. $\mu > 0$) and according to the thin-layer effect [5].

We note that the preceding weakly-nonlinear analysis can be readily adapted to the dynamics of a flow in an inclined channel. The angle of inclination would only appear in the dimensional velocity U and implicitly in the definition of $\tilde{Ca} = Ca/\epsilon = \mu_2 U/\gamma\epsilon$, therefore it would only alter the value of parameter μ in the derived model.

3. Numerical methods

A combination of analytical insight and numerical solutions of the model partial differential equation (19), as well as the direct numerical simulation solutions of the full Navier-Stokes problem (6)-(9) will be used to investigate

the flow characteristics. We begin by outlining the numerical approach used to solve the model equation (19) and providing relevant computational details on the DNS.

3.1. Model

Equation (19) is solved on a periodic domain of arbitrary length L, similar to the approach used in previous work [28]. The assumption of periodicity (justifiable here in view of the target travelling waves which would require sufficiently long pipes for spatially periodic solutions to evolve) allows us to write the solution η in the form of a Fourier series, in which case the nonlocal operator is easy to calculate. We formulate an initial value problem by introducing an initial condition in the form of a sinusoidal perturbation

$$\eta(\chi, 0) = \eta_0 \sin(k\chi), \qquad \text{with} \qquad k = \frac{2\pi\bar{k}}{L}, \tag{22}$$

where η_0 is the perturbation amplitude and $\bar{k}$ is a positive integer denoting the number of waves in one computational domain $[0, L]$. In practice, the model equation is discretised in space using spectral methods and the Fourier series is truncated by choosing suitable truncation points $|\bar{k}| < N$ such that spectral accuracy is achieved. The resulting system of ordinary differential equations for the Fourier modes is then discretised in time by applying second-order implicit-explicit Backward Differentiation Formulae [34, 35].

Travelling wave solutions are also obtained for a range of domain lengths L using a pseudo arc-length continuation method [36]. This is achieved by writing the solution in a travelling wave frame-of-reference $\eta(\chi, \tau) = \eta(\chi - c\tau)$, where c is the travelling wave speed, and solving the model equation in Fourier space (for a finite number of modes). The starting point of the continuation method is a solution obtained from a time-dependent simulation for some L, which is used as the initial guess for the Newton's method that solves the nonlinear system for a step δL along the solution branch.

3.2. Direct numerical simulations

Direct numerical simulations of the fluid system (6)-(9) are carried out using the volume-of-fluid solver *Gerris* [37, 38], whose quadtree architecture allows for efficient parallelisation and permits study of the interplay between the various physical effects in the flow. To generate the results to be presented below (including those for validation), we employed adaptive mesh

refinement, with the interfacial location, vorticity and changes in the velocity field acting as refinement criteria. A typical run would be described by $\mathcal{O}(10^5)$ grid cells depending on the aspect ratio and would be executed over 16 CPUs with a runtime of several days. As indicated in equation (4c), the pressure gradient is split into a horizontal contribution of strength G, a gravity-induced vertical variation and any additional fluid-motion-induced perturbations. To allow the use of periodic boundary conditions with a non-zero pressure gradient, the $-Gx$ contribution is added as a velocity source term of strength G to the horizontal momentum equation in each fluid layer.

Similar to what is described in equation (22), perturbations are introduced by initialising the interface between the two fluids with a given amplitude and wavenumber. However, the remaining flow quantities (e.g. the velocity and pressure) are not perturbed but are set to the base state solution. Despite the amplitude of the initial interfacial perturbation being small, this choice does nevertheless lead to an initial transient lasting several time units (a typical evolution lasts on the order of hundreds to thousands of time units) in which all the relevant quantities adjust to the imposition of the perturbation. As a simple first validation step, we have conducted verifications of the convergence to the base state solution in a stably stratified setup with different initial conditions and have observed good agreement of the relevant flow quantities when comparing to the expected two-layer Poiseuille expressions (4a)-(4c).

4. Numerical simulations

4.1. Linear regime

A linear stability analysis of the flow can be used to determine under which conditions the system is unstable. Such a study is pursued next. The model equation (19) is linearised about the uniform state $\eta = 0$ by introducing a normal-mode solution of the form $\eta(\chi, \tau) = \delta \mathrm{e}^{ik\chi+\sigma\tau}$, with $\delta \ll 1$, yielding the dispersion relation

$$\sigma = -Bo\, k^2 - k^4 - i\mu k \mathcal{V}''(1). \tag{23}$$

The term $\mathcal{V}''(1)$ is generally complex and is responsible for bringing inertial effects into the dispersion relation; it can be approximated for long waves by expanding in small powers of k in (15). The growth rate is found by the real

part of σ and is given by

$$\Re(\sigma) = \left(\frac{\mu Re}{60} \frac{8}{7} - Bo \right) k^2, \quad \text{for} \quad k \ll 1. \tag{24}$$

Long-wave instability occurs when the leading term in k is positive, which can happen in one of the following three physical scenarios: (1) for small $Re \approx 0$, inertia is negligible but the Rayleigh-Taylor instability manifests itself if the film is heavier, i.e. for $Bo < 0$; (2) for $Re > 0$ and fluids of similar densities ($Bo \approx 0$), instability arises via the thin-layer effect, namely when $\mu > 0$ and the thin film is the more viscous fluid [5]; (3) a combination of the two previous cases with instability emerging due to competing action of inertia, gravity and viscosity stratification. These remarks are in line with previously reported results regarding the stability of multilayer flows [8, 10].

As a validation case, we compare the amplification rate found above in (24) with the linear stability results of two-fluid Poiseuille flow by Yiantsios and Higgins [10]. Due to the use of different notation and dimensionalisation between the aforementioned study and this work, it is easier to perform a direct comparison by first transforming the growth rate in dimensional units. The dimensional growth rate is found to be

$$U_{max} d \left(\frac{Re}{60} \frac{16}{7} \frac{(m-1)}{m^2} - \frac{Bo}{3\tilde{Ca}} \right) \alpha^2 \epsilon^2, \tag{25}$$

where $\alpha = k/d$ is the dimensional wavenumber (only the leading-order term in α is shown). The expression in (25) is identical to the leading-order result of Yiantsios and Higgins [10] in the limit of (their depth ratio) $n \to \infty$, *i.e.* for a thin upper layer.

The predictions of the linear theory can be used to check the accuracy of numerical simulations of the asymptotic model, as well as direct numerical simulations of the full system – this was done by computing solutions in the linear regime (i.e. at early times in the simulation) and computing the growth rate as will be described next. Nonlinear simulations of the derived evolution equation (19) were performed with an initial condition of small amplitude $\eta_0 = 10^{-3}$ and of wavelength $L/\bar{k}$, where L is the domain size and $\bar{k}$ is an integer typically chosen to be $\bar{k} = 1, 2, 3$. The growth rate was then found by plotting $\log(\|\eta/\eta_0\|)$ as a function of time and estimating the slope of the straight line using first-order polynomial interpolation (here the $\|\cdot\|$ notation refers to the L_2-norm). Having obtained the growth rate $\Re(\sigma)$, we

introduce a rescaled rate s by using transformations (18) and (12), defined by

$$s = \frac{\epsilon^2}{3\tilde{Ca}} \Re(\sigma), \tag{26}$$

corresponding to the original non-dimensional time t (this transformation will also enable comparisons with DNS). Figure 2 demonstrates an example of the growth rate for $L = 8$, calculated numerically from (23); the blue dots denote the growth rate values found from the nonlinear simulation of the model equation (19) with $\bar{k} = 1, 2, 3$. Clearly the dots lie on top of the curve. In the DNS, the growth rates have been calculated by monitoring the evolution of the interfacial extrema during the early stages of the flow evolution; after the system settled into the linear regime (given that only the interfacial shape is initially perturbed, this requires several time units), a sliding least-square fit was used over the respective time window to extract the growth rates. As a sample calculation we compared the growth rates of the asymptotic model and the DNS for $\bar{k} = 2, 3$ and found $s_{MOD} \approx 0.036$ and $s_{DNS} \approx 0.032$, respectively, which clearly demonstrate a relatively good agreement. In the case $\bar{k} = 1$, the analytically obtained growth rate is small and unless we resort to a specific initial condition configuration for this scenario (e.g. significantly larger amplitudes) the fluid system tends to find one of the more unstable neighbouring wavenumber solutions first. This behaviour is consistent across a wide range of parameter values provided there is a sufficiently prominent discrepancy between the growth rates of adjacent solution points.

4.2. Nonlinear regime

In this section we present numerical solutions of the model evolution equation (19), direct numerical simulations of the full Navier-Stokes problem (6)-(9), and comparisons between the two. Unless otherwise specified we adopt the physical parameter values shown in the left column of table 1, with the corresponding dimensionless parameters given in the right column. These choices were motivated by previous studies on related two-layer shear flows [28, 29], and have been chosen to produce a stably stratified system, that is one with the lighter fluid on top. The upper fluid has been chosen to be the more viscous, and it is assumed to occupy a tenth of the channel width so that $\epsilon = 0.1$. This value of ϵ is chosen such that the asymptotic model is in its range of validity and the DNS operate in a computationally tractable regime from a multi-scale perspective (see Kalogirou et al. [28] and Figure 2

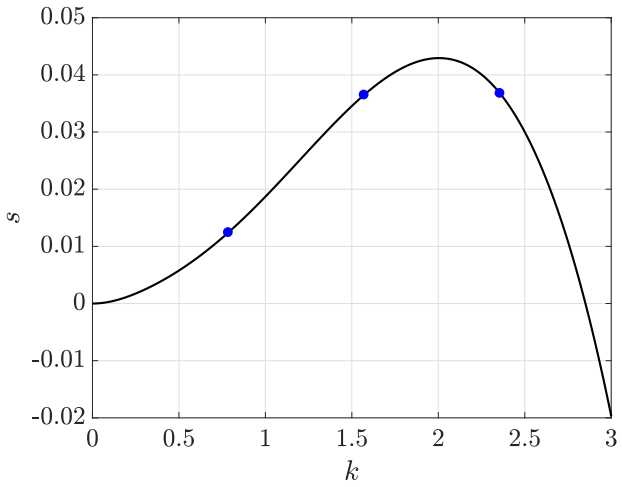

Figure 2: Growth rate found from linear dispersion relation (23) and scaled using equation (26) (solid line), and validation against nonlinear numerical computations of the model equation (19) (dots). The three dots correspond to the calculated growth rate from the nonlinear code for $\bar{k} = 1, 2, 3$ and domain length $L = 8$ (plotted at the respective values of k found from (22)). The parameter values used are as in table 1 but with the fluid densities interchanged (giving $Re = 283$, $Bo = -2.73$), hence unstable stratification is supported in this case.

therein). Referring to the dimensionless parameter values in table 1, the scaled capillary number $\tilde{Ca} = Ca/\epsilon = 1.55$ and the dimensionless viscosity stratification parameter defined in (21) takes the value $\mu = 2.15$. Accordingly the conditions required for the thin-layer effect are satisfied and we anticipate interfacial instability. The value of the Reynolds number $Re = Re_1 = 331$ indicates that we are operating in the inertial regime, where the system is susceptible to the development of interfacial travelling waves (cf. Barthelet et al. [29], Kalogirou et al. [28]) including waves of permanent form, time-periodic waves, or more complex structures [32], as will also be discussed later in this section.

To enable comparison between the numerical results obtained from the asymptotic model and the direct numerical simulations, we monitor the wave deviation from the undisturbed interfacial thickness $h_0 = 1 - \epsilon$. In the results that follow where saturated states are presented, it will be convenient to plot the saturated wave displacement as a function of time at a fixed spatial location $x = x^*$ (which can be taken to be at $x^* = 0$ or $x^* = L/2$, for example).

Physical Properties		Dimensionless Parameters	
Viscosity (1)	$\mu_1 = 0.0108$ Pa·s	Viscosity ratio	$m = 2.75$
Viscosity (2)	$\mu_2 = 0.0297$ Pa·s	Density ratio	$r = 0.85$
Density (1)	$\rho_1 = 1142$ kg/m^3	Reynolds (1)	$Re_1 = 331$
Density (2)	$\rho_2 = 975$ kg/m^3	Reynolds (2)	$Re_2 = 102.75$
Surface tension	$\gamma = 0.06$ Pa·m	Capillary	$Ca = 0.155$
Channel depth	$d = 0.01$ m	Bond	$Bo = 2.73$
Max. velocity	$U_{max} = 0.313$ m/s	Froude	$Fr = 1$
Gravity	$g = 9.81$ m/s^2	Domain length	$L = 8$ or 12

Table 1: Physical properties of the fluids used in the computations and resulting dimensionless parameters. Fluid labels 1 and 2 refer to bottom and top fluids, respectively. While these values are inspired from various types of common oils, they are not selected for a particular fluid-fluid system.

To this end we define the scaled wave amplitude $\mathcal{H}(t) = \tilde{h}(x^*, t)/\tilde{h}_{sat}$, where $\tilde{h}$ is defined in (10) and $\tilde{h}_{sat}$ is the amplitude of the saturated wave defined as half of the crest to trough distance. For convenience in comparison between the two datasets, results are shown against dimensional time measured in seconds. While a typical simulation of the nonlinear asymptotic model starting from an initial condition of the form (22) takes roughly 10 seconds to reach a saturated state, a standard DNS calculation requires several days on multiple CPUs (typically eight or sixteen) on large scale computing facilities in order to capture the same time scales. This restriction only becomes more pronounced as the film thickness ϵ is decreased into the regime in which the asymptotic model is known to perform well and the DNS become increasingly computationally expensive.

In figure 3 we present simulations that lead to saturated states that correspond to travelling waves of permanent form. The upper panels in the figure show the travelling wave signals after reaching saturation in a computational domain of size $L = 8$. The states were reached using the initial condition (22) taking $\bar{k} = 1$ so that one period of the initial disturbance wave spans the domain. The saturated travelling wave profiles found from the asymptotic model and the DNS are plotted in the upper panels of the figure and are shown over similar time windows. Evidently there is good agreement between the two in terms of wave shape, wave amplitude and period of the signal. In both cases the waves have steep crests and wide troughs with a small

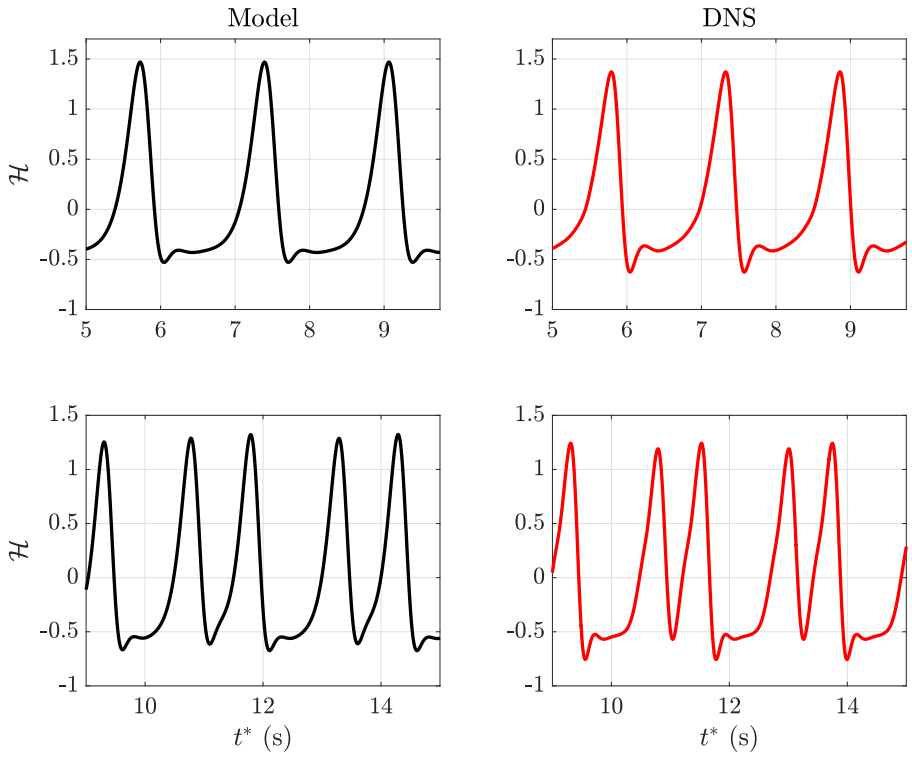

Figure 3: Time signal of the saturated wave in a channel of length $L = 8$ (top row), or $L = 12$ (bottom row), shown in dimensional time t^*. The solutions portrayed in each column are obtained from model simulations (black lines) and the DNS (red lines), respectively, both with imposed initial perturbation of wavelength equal to the domain size (i.e. $\bar{k} = 1$). The parameter values used are given in table 1.

depression preceding each trough. Noteworthy differences include a slightly larger period found with the model and a more pronounced depression in the DNS result. The results of a second simulation carried out in a larger computational domain of size $L = 12$ are shown in the bottom panels of figure 3. In this case the travelling wave signals are now more intricate. They consist of a primary wave form that is similar to those observed for shorter domains (compare the upper panels in figure 3) immediately followed by a near duplication of the main pulse. The second pulse is characterised by a shorter period than the main pulse and the absence of a depression. The asymptotic model results once again compare well with their DNS counterparts. Both solutions exhibit the discussed features although the second pulse is

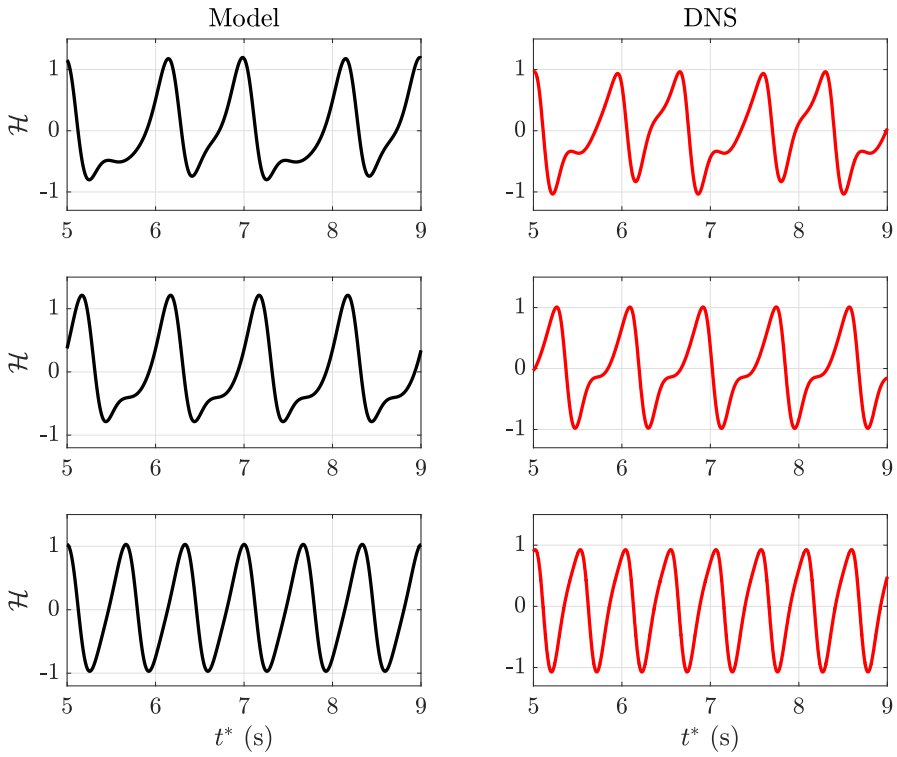

Figure 4: Saturated wave evolution in dimensional time t^* in a channel of length $L = 8$, obtained from model simulations (left panels) and the DNS (right panels) with three different initial perturbations of wavelength $\bar{k} = 1, 2, 3$ (top, middle and bottom panels, respectively). The parameter values used support unstable stratification, with $\rho_1 = 846$ kg/m^3, $\rho_2 = 1000$ kg/m^3, $\gamma = 0.07$ Pa·m, $d = 0.012$ m, yielding the dimensionless parameters $Re = 294$, $Bo = -3.12$, and $\mu = 1.84$. The rest of the parameters are as in table 1.

marginally narrower for the DNS resulting in a smaller signal period overall.

Multilayer systems like the one studied here are known to exhibit co-existence of multiple saturated wave states at the same parameter values – this phenomenon has been reported in related Couette-flow simulations [28] and also in experiments [29]. Motivated by these results we have sought solution co-existence in the present system by carrying out simulations of the asymptotic model evolution equation and DNS using three different values of $\bar{k}$ in the initial condition (22). Figure 4 presents an example case where the asymptotic model and DNS each give three distinct solutions in a domain of length $L = 8$. The solutions were obtained with initial perturbations of three

different wavelengths taking $\bar{k} = 1, 2, 3$, or equivalently $k = \frac{2\pi}{L}, \frac{4\pi}{L}, \frac{6\pi}{L}$. The agreement between the asymptotic model results shown in the left panels and the DNS in the right panels is compelling. Despite some visible differences, the same qualitative features are seen and, we emphasise, both capture the property of co-existence of solutions. The solutions on each of the three rows in the figure are characterised by having one, two or three waves in one period L, respectively, namely the number of waves that appear in one period is equal to the initial wavenumber $\bar{k}$. We note that for this particular parametric set, only the first three modes corresponding to $\bar{k} = 1, 2, 3$ are linearly unstable, and so any small amplitude perturbations of shorter wavelength are stable and will decay to the undisturbed state with a flat interface (see also the dispersion curve in figure 2). The upper panels depict the solutions dominated by the first harmonic, while in the middle and bottom panels the second and third harmonics dominate, respectively. This means that only the Fourier modes whose wavenumbers are multiples of $\bar{k}$ are unstable in each case, and that the other modes decay in time [28]. Finally, we note that the solutions from the DNS shown for $\bar{k} = 2, 3$ are obtained at relatively early times; they remain at these saturated states for a few hundred time units, but they later saturate to the $\bar{k} = 1$ profile (shown in the top right panel in figure 4).

The observed co-existence of solutions calls for a more detailed inspection of the different travelling wave solutions that appear in this multilayer system, as well as their properties. In figure 5 we show a bifurcation diagram which is obtained using the asymptotic model (19) and ~~that~~ illustrates different solution branches, characterised by the L_2-norm $\|\eta\|_2$, that are traced out as the domain length L is varied. The diagram was constructed by writing the solution in a travelling wave frame-of-reference and using arc-length continuation to follow solutions along each branch, as described in section 3.1. Results obtained from time-dependent simulations of the asymptotic model equation (19) using three different initial conditions of the form (22) with $\bar{k} = 1, 2, 3$ are superimposed using square, diamond and hexagram symbols, respectively. The bifurcation diagram reveals the existence of multiple solution branches (three shown in the figure). The first branch corresponds to unimodal solutions, i.e. solutions with a single wave in one period of the computational domain; this branch appears via a pitchfork bifurcation from the uniform steady solution $\eta = 0$ at about $L = 2.24$, below which all perturbations are stable. The second and third branches correspond to bimodal and trimodal solutions, respectively, and also emerge as pitchfork bifurcations at

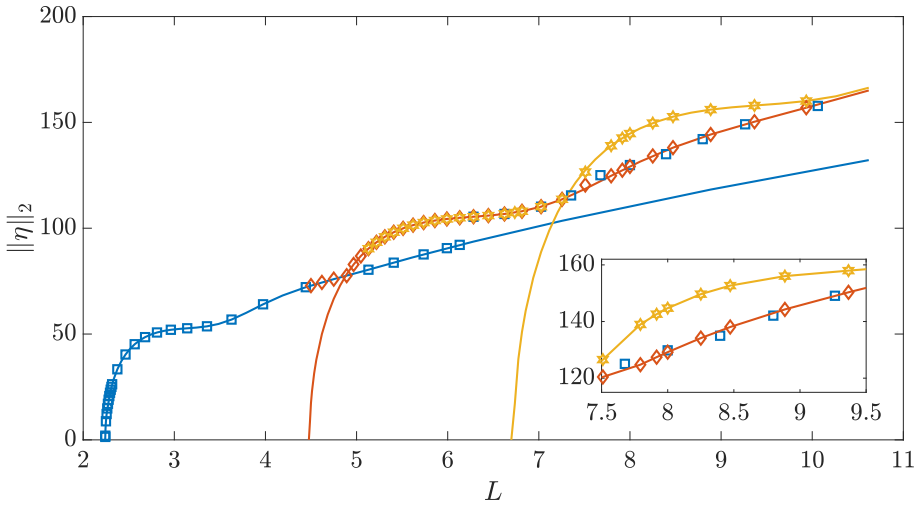

Figure 5: Bifurcation diagram of solution amplitude $\|\eta\|_2$ against domain length L. The three different branches shown with solid lines are obtained using arc-length continuation while the symbols are obtained from time-dependent simulations. The time-dependent calculations use initial condition (22) with $\bar{k} = 1, 2, 3$. Colour-symbol sets with blue-square, orange-diamond and yellow-hexagram correspond to unimodal, bimodal and trimodal initial conditions with $\bar{k} = 1, 2, 3$, respectively. The inset shows a magnification of the region $7.5 \leq L \leq 9.5$. The parameter values used are the same as in figure 4.

around $L = 4.48$ and $L = 6.7$. When the symbols along a branch appear to terminate it serves as an indication that the solutions are becoming unstable, in the sense that continuation further along the branch cannot be achieved via time-dependent calculations. One notable feature of the symbols seen in the figure is that they overlap at certain values of L, namely the same saturated solution can be obtained from time-dependent simulations with different initial conditions. For example, between approximately $L = 6.2$ and $L = 7.2$, all symbols coincide on the bimodal branch. This result has been also confirmed by DNS, with simulations reaching the same final state irrespective of the imposed initial condition. However, for longer domain lengths the three symbols become separated as the inset in figure 5 demonstrates (although visually they are hard to distinguish) and three individual solutions can be obtained – this is corroborated by the results in figure 4 for $L = 8$. It appears that there is a bifurcation on the bimodal branch that gives rise to a new branch of unimodal solutions (shown in the inset in figure 5), but we found the respective family of solutions very difficult to follow

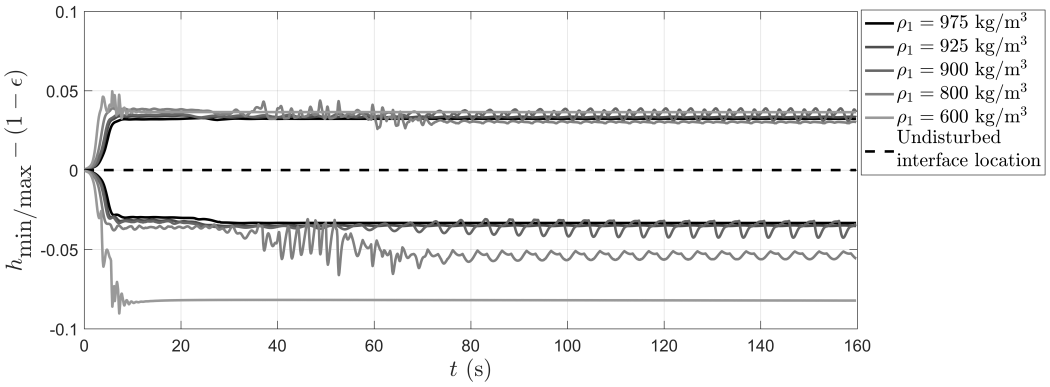

Figure 6: Time evolution of interfacial extrema for an unstably stratified system with the top fluid density fixed at $\rho_2 = 1142$ kg/m^3 and for different density bottom fluids (see legend). The remaining parameters are as given in table 1.

numerically. We conjecture the bifurcation occurs around $L = 7.4$ and the new unimodal branch reconnects to the bimodal orange branch shortly after, at around $L = 8.9$.

While the bifurcation diagram in figure 5 provides evidence on co-existence of multiple solutions, it is informative to investigate the stability of the multimodal (bimodal or trimodal) solutions when the initial condition is slightly perturbed from the respective mode. This is achieved by introducing a small-amplitude perturbation with $\bar{k} = 1$ to the initial condition (of the form $\delta \sin x$, for a chosen value of the constant δ). We found that the multimodal solutions are stable (i.e. the long-time solution is the same bimodal/trimodal solution obtained without any perturbation) as long as the perturbation amplitude is at least of the same order of magnitude or smaller than the amplitude η_0 of the original initial condition. This result serves as an indication of possible existence of the property of multistability (a feature also discovered in other related multilayer flows [16, 29]), but a more rigorous stability analysis of the various solutions is required which is not pursued further here.

Finally we discuss the behaviour of the fluid system for when the density contrast between the two fluids is increased, with the unstably stratified configuration being of primary interest. Due to the restrictions imposed on model formulations and difficulties in dealing with the topological transitions that may be involved in the very nonlinear stages of such flows, few studies have been performed in this regime (see section 1 for a summary). In what

follows we use the volume-of-fluid methodology discussed in section 3 to solve the full system (6)-(9), accounting for the high Reynolds numbers involved in the investigated flows, as well as possible interfacial rupture. Starting from the values in table 1 (but with the fluid densities flipped), we skew the competition between shear-induced and gravity-induced instabilities in favour of the latter by either keeping the density of the top fluid fixed and decreasing the density of the lower fluid or by keeping the density of the lower fluid fixed and increasing the thin film density over a range of distinct test cases spanning our chosen parameter space. The results are qualitatively similar. In figure 6 we focus on decreasing the lower fluid density as it is relevant to more realistic physical situations. For small density differences, that is for density ratios $1 < r \leq 1.25$, we find saturation to a nonlinear travelling wave. Interestingly, for an intermediate density ratio window given by $1.25 \leq r \leq 1.66$, time-periodic solutions emerge, with non-trivial but persistent features becoming visible when monitoring the interfacial extrema. This type of wave evolution has also been observed when solving the asymptotic model in equation (19); however quantitative differences are observed and direct comparisons have proven challenging in this sensitive regime. In a small interval $1.66 \leq r \lessapprox 2$ we identify rapid saturation to a nonlinear wave, while for density ratios above $r \approx 2$ multi-valued solutions begin to emerge, which are beyond the capabilities of the asymptotic model but still tractable through the direct numerical simulations.

4.3. Late-stage dynamics and break-up

Figure 7 shows a typical simulation exhibiting break-up dynamics. The fluid densities are $\rho_2 = 2000$ kg/m^3 and $\rho_1 = 846$ kg/m^3 which give a sufficiently large density ratio of $r \approx 2.364$ for rupture. The perturbation is initialised with a wavelength spanning the full domain ($\bar{k} = 1$), but, as predicted by linear stability, the more unstable $\bar{k} = 3$ wavenumber disturbance begins to dominate after the first few time steps. Irrespective of the mode of the prescribed perturbation, the linear phase of growth sees an accumulation of high density liquid towards the regions described by an initially marginally increased local thickness in the upper fluid region (see panel (a) in figure 7). Soon thereafter the nonlinear dynamics produces a complex interplay between the instability modes. Such regions are brought closer together and merging events result in a sufficiently large fluid mass to rupture the film (see panel (b) and the supplementary material for an example). The model equation (19) can no longer capture this type of dynamics due to the

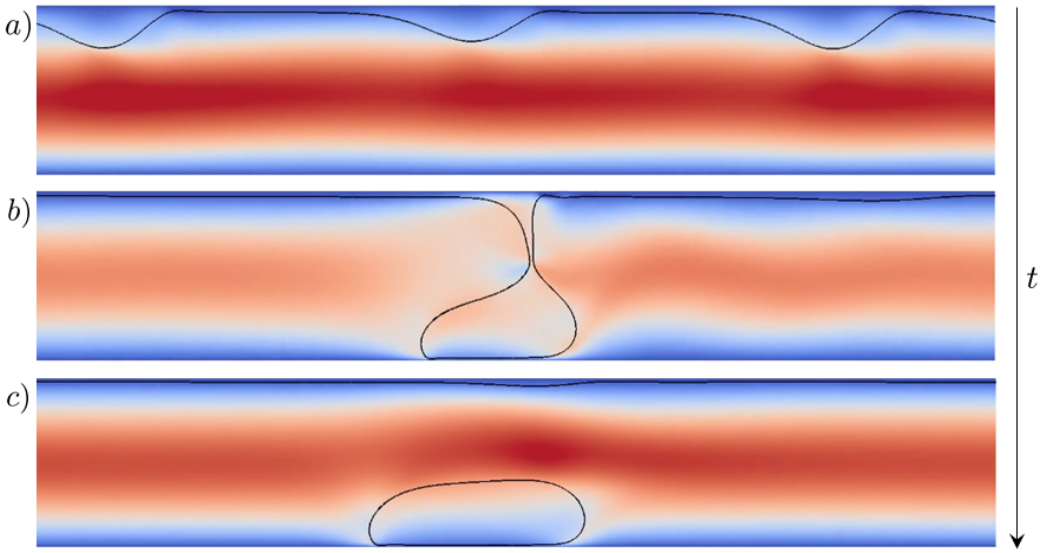

Figure 7: Snapshots of the break-up process for a test case when the density ratio is sufficiently large for rupture, with $\rho_2 = 2000$ kg/m^3 and $\rho_1 = 846$ kg/m^3. From top to bottom we see that at (a) when $t \approx 45$ the nonlinear wave is evolving leading to accumulation of fluid until (b), when $t \approx 65$, the mass accumulates sufficiently to cause a volume of the top fluid to detach, after which at (c), when $t \approx 100$, the strong flow at the centre of the channel ruptures the fluid neck. The background colour represents the strength of the horizontal velocity $u(x, y, t)$, with red indicating maxima (near the middle of the channel) and blue indicating minima (zero velocities at the channel walls). An animation of the flow during its entire evolution is provided as supplementary material.

pronounced nonlinearity and the multi-valuedness of the interfacial shape. A droplet of the upper fluid falls under gravity connected to the film by a long filament (due to sufficiently strong surface tension and confinement effects). Eventually the capillary resistance is overcome by the force exerted by the strong oncoming flow at the centre of the channel, resulting in two distinct structures: an elongated mass of fluid that becomes distorted due to the effect of gravity and the fluid motion, and a remnant liquid film at the upper wall which is sufficiently thin to prevent rupture due to surface tension (panel (c)). The remnant film is of roughly one quarter of the thickness of the initial liquid film height, with the rest of the liquid mass being lost to the detached droplet, now also being advected by the flow. We underline that the two-dimensional viewpoint becomes restrictive especially close to pinch-off due to the absence of circumferential curvature effects, for example.

We note more generally that in this unstably stratified scenario the oncoming flow acts as a shear-based stabilising mechanism competing against the gravity-induced dynamics, leading to a delay in the initial rupture, while also maintaining a stable flow once break-up has occurred. Exploration of the initial flow configuration and parameter space focusing on density ratio and amplitude of the initial perturbation in particular hint towards a rich landscape resulting in either single and multiple drop formation (not shown here for brevity). We postulate that it is possible to tailor configurations in which we can control the number of drip events by varying the geometry, the fluid properties or by the addition of external forces. This is the subject of ongoing work on related thin-film flows.

5. Discussion

We have studied a two-layer flow in a channel starting from the assumption that one of the fluid layers is thin relative to the other. In the basic state the interface between the layers is flat and the flow adopts a unidirectional Poiseuille velocity profile. Of particular interest is the nonlinear development of small amplitude disturbances to the interface. The important dimensionless parameters in the study of this problem are the capillary number, Bond number, Reynolds number, viscosity stratification, and also, in the case of a spatially-periodic disturbance as assumed here, the length of the computational domain.

Using a weakly-nonlinear analysis we have obtained an evolution equation for the film thickness which is valid for a sufficiently small amplitude disturbance. The model equation includes a nonlocal term that represents the interaction between the two layers; the contribution from the thicker layer appears via the solution of an Orr-Sommerfeld type problem for arbitrary (but not asymptotically large) Reynolds number. Using this model equation we first examined the linear stability of the flow and obtained results that are in line with the well-established physical mechanisms associated with two-fluid shear flows, namely long-wave destabilisation at non-zero Reynolds numbers [8] due to the thin-layer effect [5], and destabilisation due to density stratification [10]. The linear instabilities were followed into the weakly-nonlinear regime by performing numerical computations of the model equation on long domains (of aspect ratio 8:1 or 12:1) and for Reynolds numbers on the order of 300. We have also carried out fully nonlinear direct numerical simulations for the same parameter values to explore the range of validity of the model and

to investigate families of solutions unrestricted by modelling assumptions required as part of the derived analytical approach. The simulations for stably stratified flows indicated that the solutions are (mostly) nonlinear travelling waves of permanent form. We found good agreement between the numerical solutions of the model equation and the DNS in terms of wave amplitudes, shapes and periods. In the case of unstable stratification we found that for moderate density differences the background shear flow is able to suppress the Rayleigh-Taylor instability [15] and the interface evolves toward a saturated, stable structure. Our results have also revealed co-existence of solutions, namely the existence of multiple solutions for different initial conditions.

We have established the predictive power of the asymptotic model based on a series of comparisons between the analytical and numerical solution strategies. For regimes beyond the reach of the model (for instance when the fluids have large density differences), we have provided insight into the rich dynamical behaviour of the system by computing time-periodic travelling waves and by presenting solutions exhibiting film rupture behaviour that has not been reported before. This is the first study that presents direct comparisons between a theoretical asymptotic model and DNS of inertial pressure-driven two-layer flow. The present work can also serve as a motivation for further experimental study. Given the potential applications of the studied system in the oil and gas industry (e.g. transport of oil in pipelines [39]), it is of interest to extend this work to high Reynolds numbers, and this is the subject of ongoing work.

Acknowledgements

A.K. acknowledges funding by a Leverhulme Trust Early Career Fellowship and the Faculty of Science at the University of East Anglia. R.C. gratefully acknowledges the financial support of the Mathematical Institute at the University of Oxford in the form of the Robert Hooke Research Fellowship and the resources provided by the Imperial College Research Computing Service (DOI:10.14469/hpc/2232).

References

[1] S. Scotto, P. Laure, Linear stability of three-layer Poiseuille flow for Oldroyd-B fluids, J. Non-Newtonian Fluid Mech. 83 (1999) 71–92. doi:10.1016/S0377-0257(98)00142-6.

[2] C. Loudon, K. McCulloh, Application of the Hagen–Poiseuille equation to fluid feeding through short tubes, Ann. Entomol. Soc. Am. 92 (1999) 153–158. doi:10.1093/aesa/92.1.153.

[3] J. B. Grotberg, Pulmonary flow and transport phenomena, Annu. Rev. Fluid Mech. 26 (1994) 529–571. doi:10.1146/annurev.fl.26.010194.002525.

[4] L. Rayleigh, Investigation of the character of the equilibrium of an incompressible heavy fluid of variable density, Proc. London Math. Soc. 14 (1883) 170–177. doi:10.1112/plms/s1-14.1.170.

[5] A. P. Hooper, Longwave instability at the interface between two viscous fluids: Thin layer effects, Phys. Fluids 28 (1985) 1613–1618. doi:10.1063/1.864952.

[6] M. E. Charles, L. U. Lilleleht, An experimental investigation of stability and interfacial waves in a co-current flow of two liquids, J. Fluid Mech. 22 (1965) 217–224. doi:10.1017/S0022112065000691.

[7] T. W. Kao, C. Park, Experimental investigations of the stability of channel flows. Part 2. Two layered co-current flow in a rectangular channel, J. Fluid Mech. 52 (1972) 401–423. doi:10.1017/S0022112072001508.

[8] C.-H. Yih, Instability due to viscosity stratification, J. Fluid Mech. 27 (1967) 337–352. doi:10.1017/S0022112067000357.

[9] S. G. Yiantsios, B. G. Higgins, Numerical solution of eigenvalue problems using the compound matrix method, J. Comput. Phys. 74 (1988) 25–40. doi:10.1016/0021-9991(88)90066-6.

[10] S. G. Yiantsios, B. G. Higgins, Linear stability of plane Poiseuille flow of two superposed fluids, Phys. Fluids 31 (1988) 3225–3238. doi:10.1063/1.866933.

[11] P. J. Blennerhassett, On the generation of waves by wind, Philos. T. Roy. Soc. A 298 (1980) 451–494. doi:10.1098/rsta.1980.0265.

[12] A. P. Hooper, The stability of two superposed viscous fluids in a channel, Phys. Fluids 1 (1989) 1133–1142. doi:10.1063/1.857338.

[13] Y. Renardy, Viscosity and density stratification in vertical Poiseuille flow, Phys. Fluids 30 (1987) 1638–1648. doi:10.1063/1.866228.

[14] N. R. Anturkar, T. C. Papanastasiou, J. O. Wilkes, Linear stability analysis of multilayer plane Poiseuille flow, Phys. Fluids 2 (1990) 530–541. doi:10.1063/1.857753.

[15] B. S. Tilley, S. H. Davis, S. G. Bankoff, Linear stability theory of two-layer fluid flow in an inclined channel, Phys. Fluids 6 (1994) 3906–3922. doi:10.1063/1.868382.

[16] B. S. Tilley, S. H. Davis, S. G. Bankoff, Nonlinear long-wave stability of superposed fluids in an inclined channel, J. Fluid Mech. 277 (1994) 55–83. doi:10.1017/S0022112094002685.

[17] H. Power, M. Villegas, C. Carmona, Nonlinear inertial effects on the instability of a single long wave of finite amplitude at the interface of two viscous fluids, J. Appl. Math. Phys. (ZAMP) 42 (1991) 663–679. doi:10.1007/BF00944765.

[18] I. Kliakhandler, G. Sivashinsky, Inertial effects and long waves in multilayer plane Poiseuille flows, Phys. Scripta T67 (1996) 90–95. doi:10.1088/0031-8949/1996/T67/018.

[19] M. Sangalli, M. J. McCready, H.-C. Chang, Stabilization mechanisms of short waves in stratified gas-liquid flow, Phys. Fluids 9 (1997) 919–939. doi:10.1063/1.869188.

[20] K. Alba, P. Laure, R. E. Khayat, Transient two-layer thin-film flow inside a channel, Phys.Rev. E 84 (2011) 1–14. doi:10.1103/PhysRevE.84.026320.

[21] A. B. Thompson, S. N. Gomes, G. A. Pavliotis, D. T. Papageorgiou, Stabilising falling liquid film flows using feedback control, Phys. Fluids 28 (2016) 1–30. doi:10.1063/1.4938761.

[22] Q. Cao, K. Sarkar, A. K. Prasad, Direct numerical simulations of two-layer viscosity-stratified flow, Int. J. Multiph. Flow 30 (2004) 1485–1508. doi:10.1016/j.ijmultiphaseflow.2004.07.005.

[23] J. Zhang, M. J. Miksisa, S. G. Bankoff, G. Tryggvason, Nonlinear dynamics of an interface in an inclined channel, Phys. Fluids 14 (2010) 1877–1885. doi:10.1063/1.1475313.

[24] V. Gada, A. Sharma, Analytical and level-set method based numerical study on oil-water smooth/wavy stratified-flow in an inclined plane-channel, Int. J. Multiphase Flow 38 (2012) 99–117. doi:10.1016/j.ijmultiphaseflow.2011.08.015.

[25] P. Valluri, L. O. Naraigh, H. Ding, P. D. M. Spelt, Linear and nonlinear spatio-temporal instability in laminar two-layer flows, J. Fluid Mech. 656 (2010) 458–480. doi:10.1017/S0022112010001230.

[26] T. I. Hesla, F. R. Pranckh, L. Preziosi, Squire's theorem for two stratified fluids, Phys. Fluids 29 (1986) 2808–2811. doi:10.1063/1.865478.

[27] K. C. Sahu, O. K. Matar, Three-dimensional convective and absolute instabilities in pressure-driven two-layer channel flow, Int. J. Multiphase Flow 37 (2011) 987–993. doi:10.1016/j.ijmultiphaseflow.2011.05.005.

[28] A. Kalogirou, R. Cimpeanu, E. E. Keaveny, D. T. Papageorgiou, Capturing nonlinear dynamics of two-fluid Couette flows with asymptotic models, J. Fluid Mech. 806 (2016) R1. doi:10.1017/jfm.2016.612.

[29] P. Barthelet, F. Charru, J. Fabre, Experimental study of interfacial long waves in a two-layer shear flow, J. Fluid Mech. 303 (1995) 23–53. doi:10.1017/S0022112095004162.

[30] A. P. Bassom, M. G. Blyth, D. T. Papageorgiou, Nonlinear development of two-layer Couette-Poiseuille flow in the presence of surfactant, Phys. Fluids 22 (2010) 1–15. doi:10.1063/1.3488226.

[31] A. Kalogirou, Instability of two-layer film flows due to the interacting effects of surfactants, inertia, and gravity, Phys. Fluids 30 (2018) 1–12. doi:10.1063/1.5010896.

[32] D. T. Papageorgiou, C. Maldarelli, D. S. Rumschitzki, Nonlinear interfacial stability of core-annular film flows, Phys. Fluids 2 (1990) 340–352. doi:10.1063/1.857784.

[33] A. Kalogirou, Nonlinear dynamics of surfactant-laden multilayer shear flows and related systems, Ph.D. thesis, Imperial College London, 2014. Available from: https://spiral.imperial.ac.uk/handle/10044/1/25067.

[34] G. Akrivis, Y.-S. Smyrlis, Linearly implicit schemes for a class of dispersive–dissipative systems, Calcolo 48 (2011) 145–172. doi:10.1007/s10092-010-0033-6.

[35] G. Akrivis, D. T. Papageorgiou, Y.-S. Smyrlis, Computational study of the dispersively modified Kuramoto–Sivashinsky equation, SIAM J. Sci. Comput. 34 (2012) A792–A813. doi:10.1137/100816791.

[36] E. J. Doedel, Lecture notes on numerical analysis of nonlinear equations, in: B. Krauskopf, H. M. Osinga, J. Galan-Vioque (Eds.), Numerical Continuation Methods for Dynamical Systems, Understanding Complex Systems, Springer, United Kingdom, 2007.

[37] S. Popinet, Gerris: A tree-based adaptive solver for the incompressible Euler equations in complex geometries, J. Comput. Phys. 190 (2003) 572–600. doi:10.1016/S0021-9991(03)00298-5.

[38] S. Popinet, An accurate adaptive solver for surface-tension-driven interfacial flows, J. Comput. Phys. 228 (2009) 5838–5866. doi:10.1016/j.jcp.2009.04.042.

[39] D. D. Joseph, R. Bai, K. P. Chen, Y. Y. Renardy, Core-annular flows, Annu. Rev. Fluid Mech. 29 (1997) 65–90. doi:10.1146/annurev.fluid.29.1.65.